Journal of
Microscopy

Journal of Microscopy, Vol. 243, Pt 1 2011, pp. 77–85
Received 19 October 2010; accepted 19 December 2010
doi: 10.1111/j.1365-2818.2010.03483.x

Revealing the 3D internal structure of natural polymer microcomposites using X-ray ultra microtomography

A. PAKZAD*, N. PARIKH*, P.A. HEIDEN† & R.S. YASSAR*
**Mechanical Engineering-Engineering Mechanics, Michigan Technological University, Michigan, U.S.A.*
†Department of Chemistry, Michigan Technological University, Michigan, U.S.A.

Key words. Cellulose, dispersion, mechanical properties, polymer, X-ray ultra microscopy.

Summary

Properties of composite materials are directly affected by the spatial arrangement of reinforcement and matrix. In this research, partially hydrolysed cellulose microcrystals were used to fabricate polycaprolactone microcomposites. The spatial distribution of cellulose microcrystals was characterized by a newly developed technique of X-ray ultra microscopy and microtomography. The phase and absorption contrast imaging of X-ray ultra microscopy revealed two-dimensional and three-dimensional information on CMC distribution in polymer matrices. The highest contrast and flux (signal-to-noise ratio) were obtained using vanadium foil targets with the accelerating voltage of 30 keV and beam current of >200 nA. The spatial distribution of cellulose microcrystals was correlated to the mechanical properties of the microcomposites. It was observed that heterogeneous distribution and clustering of cellulose microcrystals resulted in degradation of tensile strength and elastic modulus of composites. The utilization of X-ray ultra microscopy can open up new opportunities for composite researchers to explore the internal structure of microcomposites. X-ray ultra microscopy sample preparation is relatively simple in comparison to transmission electron microscopy and the spatial information is gathered at much larger scale.

Introduction

Among various natural reinforcements, much interest has been devoted to the usage of polysaccharides such as chitin, starch and cellulose. Cellulose is the most abundant naturally occurring polymer on earth, and is produced and recycled at a rate of 10^{10} tons year^{-1} (Hon, 1994). It is most widely found in plants (Fleming *et al.*, 2000; Habibi *et al.*, 2008; Siqueira *et al.*, 2009), but some animals (Angles & Dufresne, 2000) and bacteria (Grunert & Winter, 2002) are also sources of cellulose.

Cellulose consists of both crystalline and amorphous domains. Although the amorphous part enables deformation, the crystalline part provides the strength, density and rigidity (Hamad, 2006). The reinforcing efficiency of cellulose depends on the fraction of crystalline domains and their interaction with the domain that they are reinforcing (Lapa *et al.*, 2007). Native cellulose subjected to strong acid hydrolysis readily breaks down into micro- or nanocrystals (Batista, 1975).

Despite the above-mentioned attractive properties, the lack of control over the dispersion of cellulose crystals in polymer matrices has limited their use in the composite industry (Oksman *et al.*, 2006). Cellulose is a hygroscopic linear polysaccharide of β-D-glucopyranose units, which are connected by (1→4)-glycosidic bonds. The strong intermolecular hydrogen bonding forces, arising from the hydroxyl groups on the cellulose chains, cause a major fabrication difficulty. The hydrophilic nature of cellulose and the nonpolar characteristics of most thermoplastics make it difficult to achieve a sufficient dispersion of this reinforcement in polymer matrices.

Conventional methods for characterization of microstructures in composite materials are generally limited to study of the surface or a localized portion of the composite volume. In addition, they often require tedious sample preparation steps, or they are complex in the sense of data interpretation. These methods include: optical microscopy (Wang & Sain, 2007), scanning electron microscopy (SEM) (Choi & Simonsen, 2006), transmission electron microscopy (Bodenson & Oksman, 2007), atomic force microscopy (Matsumura & Glasser, 2000), small angle X-ray scattering (Mele *et al.*, 2002) and wide angle X-ray diffraction (Vaia & Liu, 2002).

Correspondence to: Reza S. Yassar, Mechanical Engineering-Engineering Mechanics, Michigan Technological University, 1400 Townsend Dr., Houghton, MI 49931, U.S.A. Tel: +1-(906)-487-3581; e-mail: reza@mtu.edu

Recently, a technique of X-ray ultra microscopy (XuM) and microtomography has been developed, which offers the capability of observing the internal structure of opaque materials at submicron scales. The idea of X-ray projection microscopy originated in the 1950s (Cosslett & Nixon, 1951; Nixon, 1955), but such systems were developed and made usable only in the last decade (Mayo *et al.,* 2002, 2003). Tomography has been performed in various media, for example, acoustic waves (Maurer *et al.,* 2006) or neutrons (Dierick *et al.,* 2005) and X-rays. Some other examples of current techniques established for X-ray microcomputed tomography are: synchrotron X-ray tomography (with less than one μm^3 resolution) (Bonse & Bush, 1996; Laiarinandrasana *et al.*, 2010) and laboratory desktop microtomography, which can reach down to 5 μm spatial resolution (Weiss *et al.,* 2005). The differences between these methods are the X-ray generation source, X-ray source–sample–detector configuration, imaging resolution and acquisition time. The resolution of XuM will be discussed in section 'Selection of target material and 3D reconstruction'.

X-ray computed tomography has many interesting applications in different research areas. In the field of polymers, for instance, it has been used to study the void volume fraction in necking region of tensile test specimens (Laiarinandrasana *et al.,* 2010). XuM is well suited to examine the quality of dispersion of reinforcements in polymer composites. Other attractive advantages over conventional microscopy techniques include easier sample preparation, the nondestructive nature of analysis and the ability to obtain large-scale statistical information of the internal structure.

Given the difficulties associated with quantification of cellulose dispersion in polymer matrices, in this study, XuM was used to study the internal structure of partially hydrolysed cellulose microcrystals (CMC) dispersed in polycaprolactone (PCL). CMC and PCL have low chemical compatibility and because the surface of PCL or CMC were not chemically modified, thus a homogeneous dispersion and mechanical reinforcement were not expected. The main focus of this work is to demonstrate the applicability of XuM to reveal the 3D views of CMC clustering and tangling within PCL matrix. A direct correlation between the bulk mechanical properties and the XuM data was also made. The results demonstrate the feasibility of this technique for dispersion quality analysis of other natural polymer composites.

Materials and methods

Cellulose composite film preparation

PCL was selected as the matrix to prepare composite films. PCL is a linear hydrophobic polyester, which is synthetically produced and is biodegradable. Commercially available CMC, produced by sulphuric acid treatment of bleached Kraft wood fibres followed by washing and drying, was partially hydrolysed and used at 0, 10, 30 and 50 wt.%. Hereafter, these composites are named PCL 0, PCL 10, PCL 30 and PCL 50, respectively. Sulphuric acid hydrolysis of the CMCs was done under moderate conditions. The hydrolysis was insufficient to give nanocrystals but did begin the defibrillation process. In summary, 5.6 g commercially available CMC was placed in 64% H_2SO_4 solution for 1 h at 45°C with medium stirring. The cellulose-to-acid ratio was 1:10. After 45 min, deionized water was added to the solution to stop the reaction. Afterwards, centrifugation at 2330 g was used to wash the solids until a neutral pH was obtained (IEC DPR-6000 centrifuge). Next, the solids were placed in dialysis bags and washed against deionized water for several days.

Evenly dispersion of cellulose in PCL matrix is critical for improvement of mechanical properties. Because cellulose is polar and PCL is nonpolar, this is only possible if the surface polarity of CMC is changed (Siqueira *et al.,* 2009) or if PCL is directly grafted to CMC (Habibi & Dufresne, 2008). The goal here was not to improve the mechanical properties, but to characterize the distribution of CMC in PCL. Thus, composite films were prepared by simple mixing and without any chemical modification of CMC or PCL.

Partially hydrolysed CMCs were dispersed in $CHCl_3$ and sonicated for 0.5 h. Separately, PCL was dissolved in $CHCl_3$ and then mixed with the sonicated crystals, as they were vigorously stirred with a mechanical stirrer. The stirring was continued for 2 h after the addition was completed. Afterwards, the solvent was removed under reduced pressure at 60°C, and the combination was transferred into moulds and heated at 140°C under 20 MPa pressure, for 10 min.

Mechanical testing

Mechanical characterization of the polymer composites was carried out using an MTS universal testing machine with a 4.5 kN load cell. All samples were cut in equal rectangular shapes. The gage length dimensions of the samples were $0.7 \times 4 \times 6$ mm^3, and at least three tests were performed with each composition to work around any experimental scatter. Load was applied by moving the cross head with 0.127 cm min^{-1} rate. Load–displacement curves were obtained and converted to engineering stress–strain curves using the initial length and area of each sample. Reported ultimate tensile strength (UTS) values are average values of at least three tests (Table 1).

Table 1. The UTS values in PCL microcomposites.

CMC content (wt.%)	UTS (MPa)
0	17.48 ± 0.33
10	14.55 ± 0.16
30	10.3 ± 0.21
50	7.55 ± 2.76

Morphological analysis

XuM work was carried out at Gatan Inc. (Pleasanton, CA, USA). The XuM set-up was installed in a Hitachi S-3400 N SEM. The main components, shown in Fig. 1(a), are a rotation stage, charge-coupled detector (CCD) X-ray camera and a target module, which positions up to five metal targets and allows operating X-ray microscopy inside a SEM. In this method, the X-ray images are obtained by focusing the electron beam on a metal target, and passing the generated X-rays through the sample. Adopting the point projection geometry principles, 2D X-ray images can be recorded. To obtain a 3D visualization, 2D images are taken as the sample rotates in small angle increments, and then the projections are computationally combined (see section 'Selection of target material and 3D reconstruction').

To acquire 2D images, a very small X-ray source is created on a thin metal target by focusing the electron beam (Fig. 1b). A sample is then placed between the source and the charge-coupled detector. This results in a simple point projection geometry (Cosslett & Nixon, 1960), where X-rays pass through the specimen and create a magnified image on the detector. Usually, the source to sample distance (R_1) is much smaller than the source to detector distance (R_2) and this enables magnifications ($M = R_2/R_1$) up to 2000×. Depending on the electron beam energy and the target material, X-ray energy may vary between 4 and 12 keV. Imaging resolution greatly depends on the X-ray source size (Goldstein *et al.*, 2003), and can be as small as 200 nm in 2D and 1 μm in 3D.

Because of the small source size and R_1, in-line phase contrast is obtained on the image plane, in addition to absorption contrast, as a result of near-field Fresnel diffraction

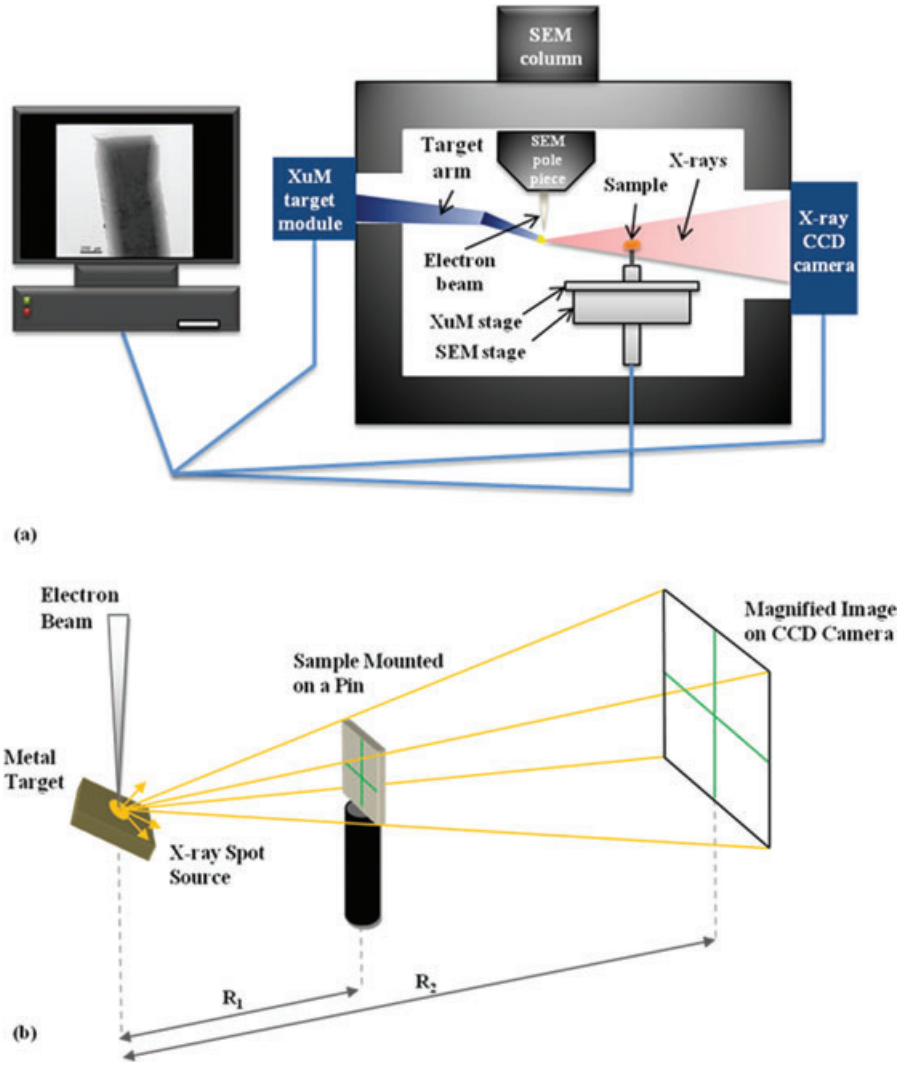

Fig. 1. (a) Main components of the XuM inside SEM, to generate X-rays, a metal target is positioned under the electron beam using the target module. X-rays pass through the sample and create the 2D image on the charge-coupled detector camera. (b) Point projection geometry in XuM; the magnification ($M = R_2/R_1$) can be changed by moving the sample towards or away from the X-ray source.

(Mayo *et al.*, 2003; Myers *et al.*, 2008). Phase contrast enhances the visibility of boundaries, voids and edges and is critical for weakly or nonabsorbing samples, such as polymers.

Selection of target material and 3D reconstruction

The resolution and energy of X-rays are directly related to the choice of target material, and thus a systematic study was performed to select an appropriate target. For this purpose, a graph of accelerating voltage versus intensity of 11 metal targets, along with the imaging resolution at each point was created (Fig. 2). To generate this graph, NIST/NIH Desktop Spectrum Analyser was used to create X-ray spectra (intensity vs. accelerating voltage) generated by the targets under various accelerating voltages. The highest peaks on these spectra were then used as intensities. These intensities were normalized relative to the intensity of X-rays generated by W at 30 keV, and are shown on the vertical axis.

Anderson–Hasler X-ray range (R) was used as the imaging resolution (X-ray source size) for each metal (Goldstein *et al.*, 2003). Resolution is shown by the diameter of the circles on the graph and depends on the incident energy (E_c) and the material properties of the target (ρ = density, E_0 = critical excitation energy):

$$R = \frac{0.064}{\rho}(E_0^{1.68} - E_c^{1.68}).$$

The choice of target material and the accelerating voltage of the SEM are two major parameters that affect the resolution (shown as the size of circles with diameters of less than 2 μm), and the intensity of X-rays, and in-turn the quality of XuM data. It can be seen from Fig. 2 that higher accelerating voltage results in higher intensities but reduction in maximum resolution at the same time. For instance, in the case of V, when the accelerating voltage is increased from 10 to 30 keV, the relative intensity increases almost 14 times but the theoretical resolution changes from 0.16 to 1.50 μm.

Next, four metal targets namely Ag, V, W and Au were selected to experimentally examine their ability to enhance the contrast of specific features in a sample. Samples were mounted on Al pins and coated with 20 nm Pt in a Gatan precision etching coating system. Then 2D X-ray images were acquired using these metal targets and various accelerating voltages (10–30 keV). The best quality images with the highest contrast and flux (signal-to-noise ratio, S/N), were obtained using V foil target with an accelerating voltage of 30 keV, and beam current of >200 nA (Fig. 3).

To produce a 3D reconstruction for each sample, a tomographic dataset containing 190 2D projections with one-degree increments between each projection was obtained. To acquire the adequate signal to noise ratio (S/N > 2), each projection consisted of at least three frames, with minimum of 10 s exposure time. These images are then back projected using a cone-beam back projection algorithm (Feldkamp *et al.*, 1984) to create a 3D image of the volume.

Results and discussion

Fig. 4 shows the typical engineering stress–strain curves obtained for the microcomposite samples, whereas Table 1

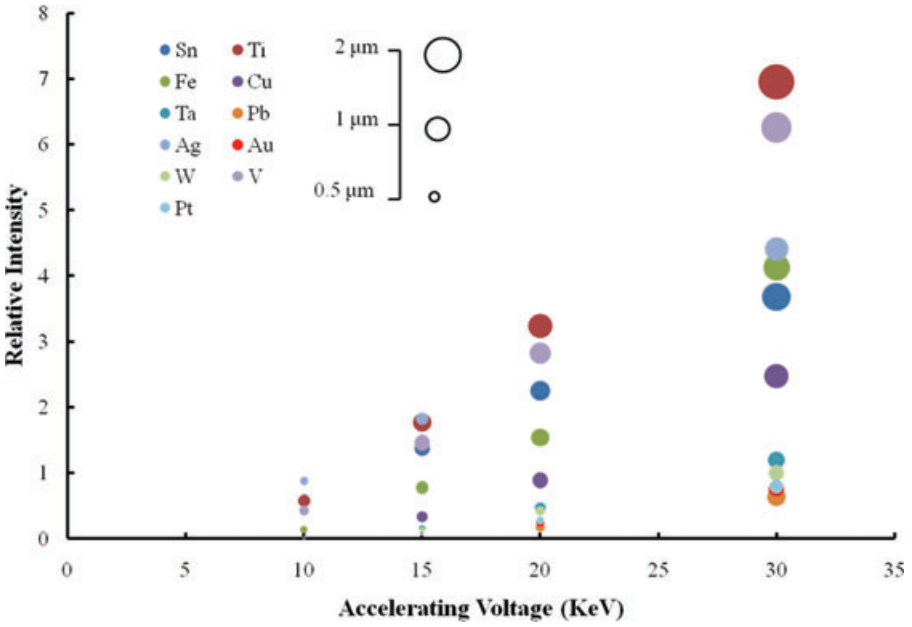

Fig. 2. Relative intensity and resolution of XuM metal targets. The diameter of the circles on the graph represents the imaging resolution in micrometres. Intensities were reported relative to intensity of *W* at 30 keV.

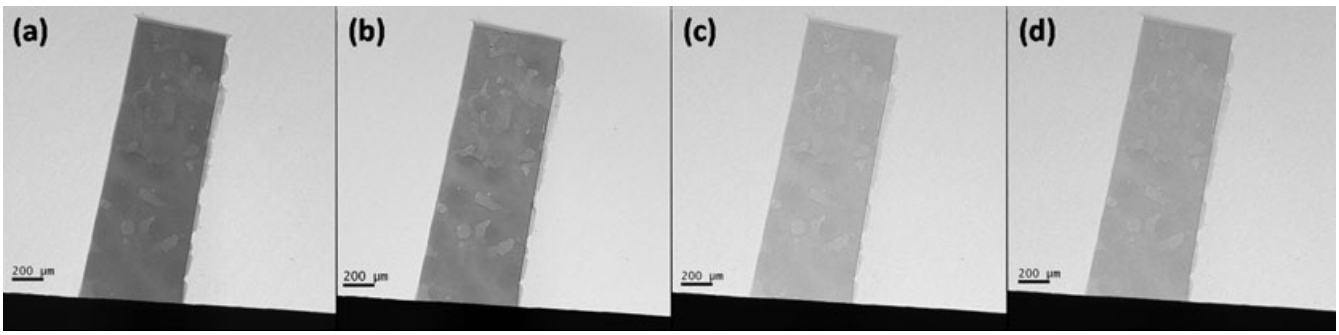

Fig. 3. 2D XuM images of PCL samples obtained under (a) Ag, (b) V, (c) W and (d) Au metal targets. The accelerating voltage was fixed at 30 keV. The choice of V target was preferred because of its optimal contrast and flux.

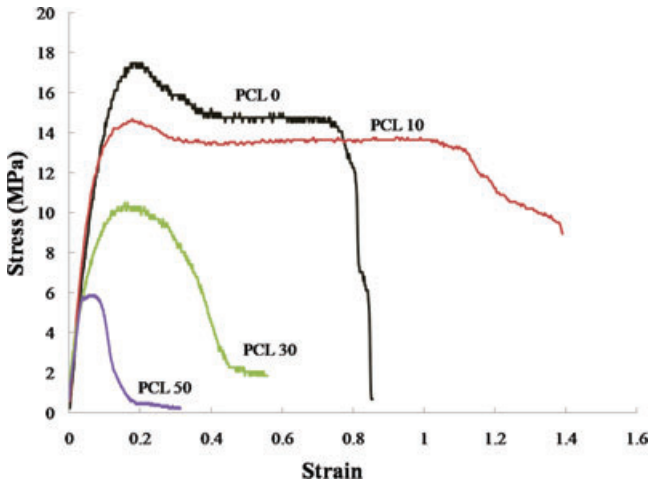

Fig. 4. Engineering stress–strain curves for PCL composites: black: PCL 0, red: PCL 10, green: PCL 30 and purple: PCL 50.

summarizes the tensile test results as ultimate tensile stress (UTS). Addition of CMC to PCL degraded the UTS. As the amount of CMC increased from 0 to 50 wt.%, the UTS decreased from 17.48 to 5.5 MPa (=68% decrease). No major changes were observed in the elastic modulus, but as the amount of CMC was increased, the yield stress appeared to decrease in PCL composites.

An important observation is that the plateau of stress–strain curves almost disappeared in PCL 30 and PCL 50, yet this range was the highest in PCL 10. Because of lack of good adhesion between polar CMC and nonpolar PCL, at high concentration of CMCs (30 and 50 wt.%), debonding at the CMC and PCL interface is the governing mechanism, while at 10 wt.%, the CMCs underwent reorientation along with sliding of polymer chains, which accounted for the large deformation plateau in the PCL10 samples.

Fractography of the PCL composites was carried out using a Hitachi S-4700 field emission SEM operating under a voltage of 3 keV (Fig. 5). Although only one SEM image is shown here, for each composition, at least four fracture surfaces were studied. Relatively smooth surfaces were observed in PCL 0 and PCL 10 samples (Figs. 5a and b). As the amount of CMC increased, the fracture surface became rougher and more voids and ridges could be detected (Figs. 5c and d). PCL with 30 wt.% CMC appeared to have many voids, which may be areas where CMCs debonded during tensile experiments. The fracture surface of PCL 50 showed the roughest surface.

The correlation of fractography data and stress–strain curves revealed two competing mechanisms during the deformation of CMC–polymer composites. The reduction of UTS in all the CMC-samples indicates that the bonding between CMCs and polymer matrix was weak. However, in PCL 10, CMCs have successfully rendered the void coalescence and therefore allowed the movement of polymer molecular chains up to higher strains. At 30% and 50% CMC content, the void population increases due to the higher number of debonding incidents, and therefore void-assisted fracture dominated the deformation of composites.

The 2D X-ray images of the samples are shown in Fig. 6 (similar to fractography, for each composition, multiple samples were prepared and studied in the XuM). X-ray images show the dispersion of CMC through the specimens. Good contrast on CMC distribution was obtained for specimens, because the difference between X-ray absorption of PCL and CMC is high enough and as a result there is difference in the intensity of regions corresponding to PCL or CMC in the images. In addition to absorption contrast, phase contrast accentuated both the interphase regions and the cracks.

Fig. 7 shows the 3D reconstruction of a composite sample. CMC appeared as higher density regions in the back projections. After reconstruction, any horizontal or vertical slice through the sample can be studied (Figs. 7a and b). These planes can be simultaneously visualized with the 3D volume as shown in Fig. 7(c).

Fig. 8 depicts the PCL specimens in 3D. PCL and CMC are shown in grey and green colours, respectively. As can be seen, some regions of the reinforced samples have clusters of CMCs whereas other regions are purely PCL. This correlates directly to degradation of UTS as the CMC content is increased. Because

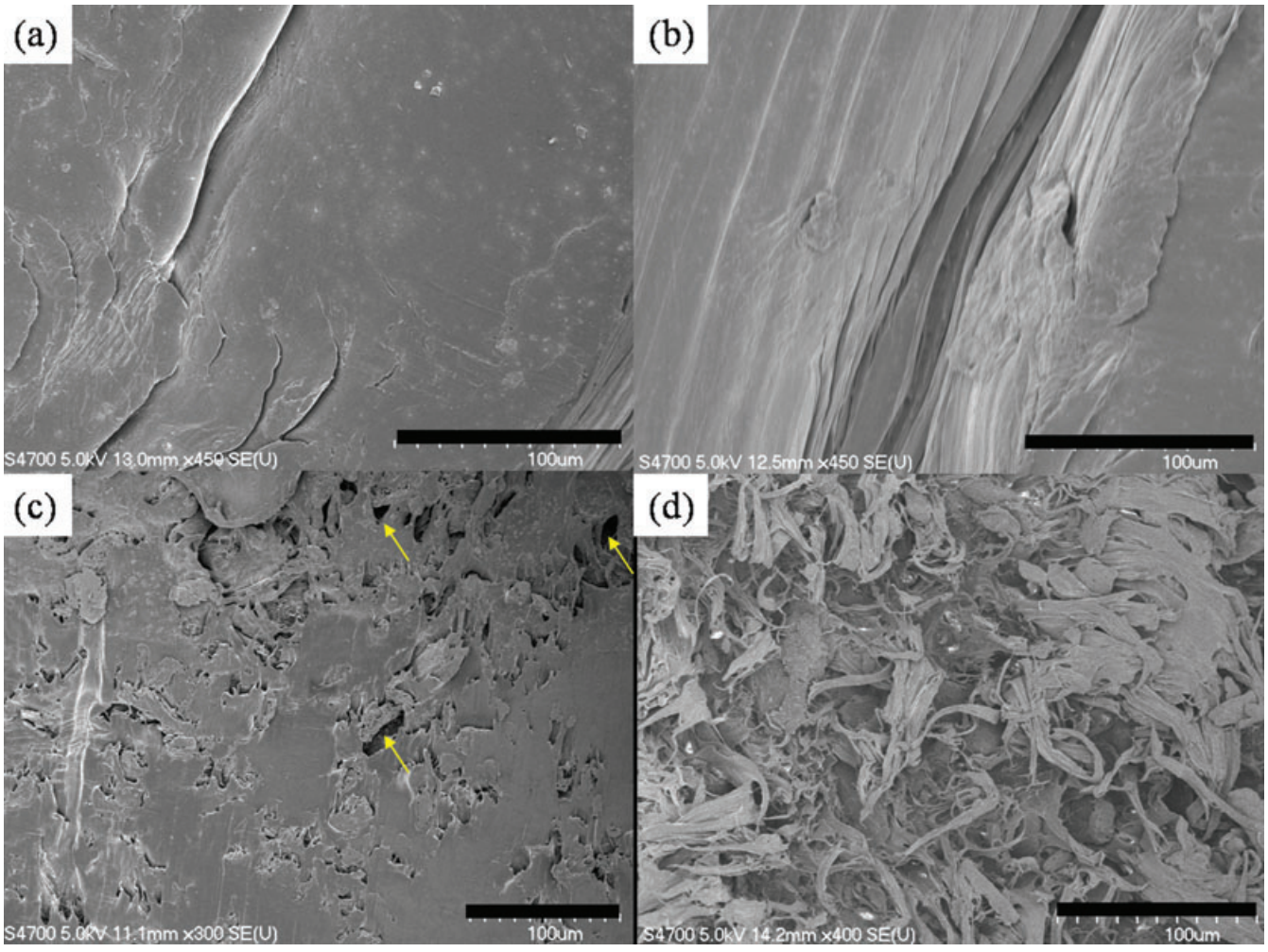

Fig. 5. SEM images from the fracture surface of CMC–PCL composites: (a) PCL 0, (b) PCL 10, (c) PCL 30 and (d) PCL 50. Arrows in (c) show voids that were created as a result of CMC being pulled out during the tensile test. (Scale bars are 100 μm.)

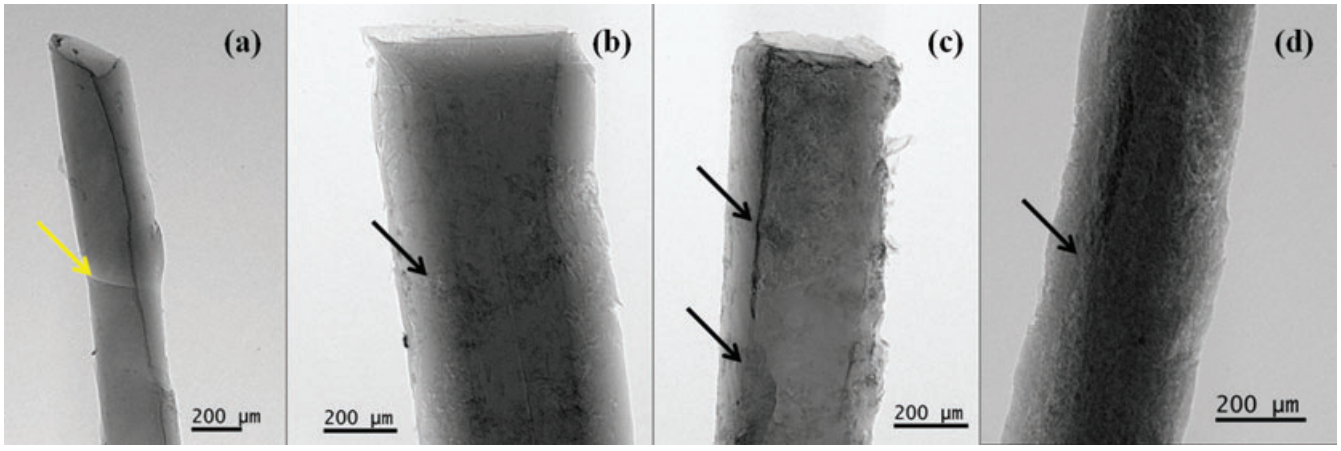

Fig. 6. 2D XuM images of PCL composites: (a) PCL 0, (b) PCL 10, (c) PCL 30 and (d) PCL 50. Some of the CMCs are shown by black arrows on the images. The yellow arrow in (a) shows a crack in the sample, which was created during sample preparation (phase contrast). (Scale bars are 200 μm.)

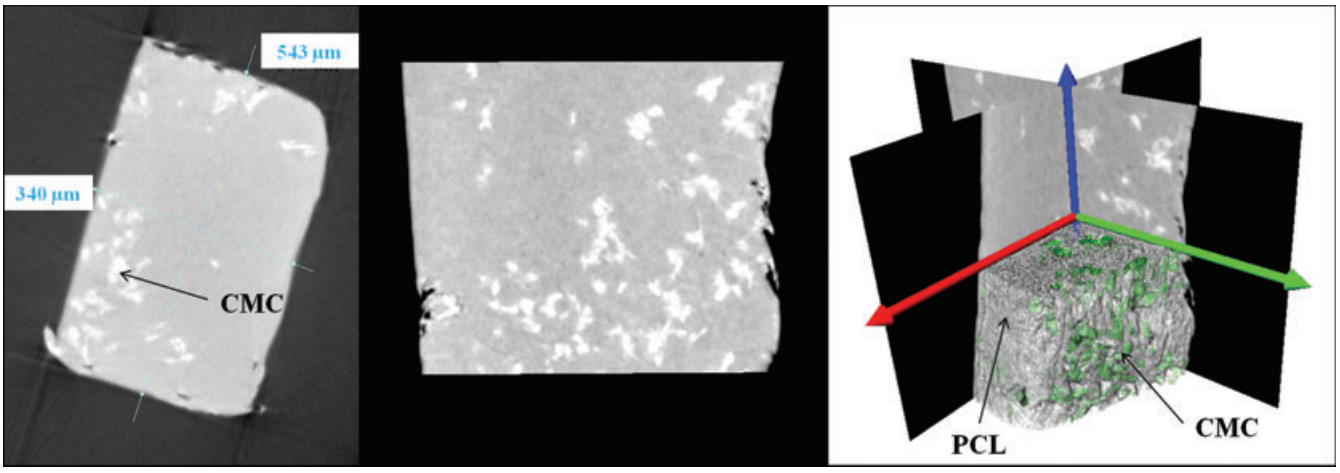

Fig. 7. 3D reconstruction of a PCL sample filled with 10 wt.% CMC. CMC can be recognized as bright regions. (a) Horizontal slice of 340 by 543 μm^2 through the sample. (b) Vertical plane through the specimen. (c) 3D volume is shown along with two slices through the sample. PCL and CMC are shown as gray and green zones.

of the weak interface bonding, these clusters act as stress concentration points, where debonding and fracture start. Microfractures and voids propagate as the stress increases and they ultimately result in the failure of the material.

To study the size and distribution of CMCs, statistical analyses on the cluster diameter, aspect ratio and orientation distributions were obtained on a single vertical plane through the sample (Fig. 9). In this work, the cluster diameter was assumed to be equal to an equivalent cluster diameter ($C\,D = 2\sqrt{\frac{A}{\pi}}$) calculated from the area (A) of particles (Jennings & Parslow, 1988).

In literature, there are numerous studies on the effect of reinforcement geometry and concentration on the mechanical properties of polymer composites (Choi & Simonsen, 2006; Bodenson & Oksman, 2007). The 3D characterization by XuM enables one to access such statistical information on the

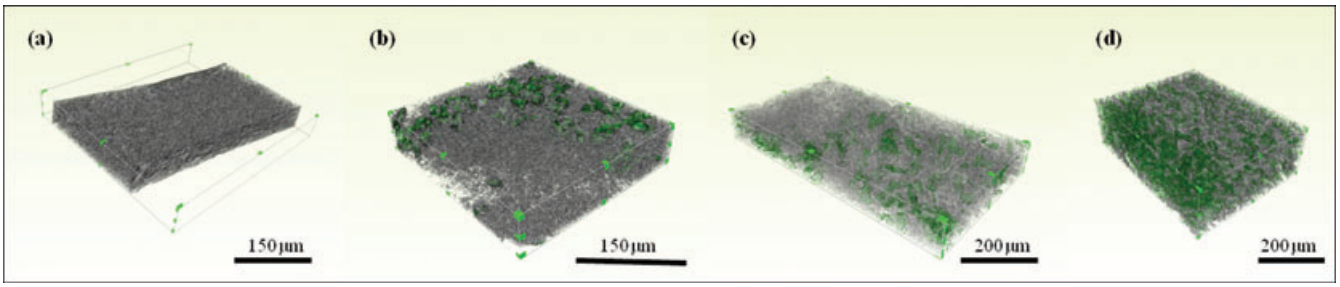

Fig. 8. 3D visualization of PCL samples filled with (a) 0 wt.%, (b) 10 wt.%, (c) 30 wt.% and (d) 50 wt.% CMCs. PCL and CMCs are shown in grey and green, respectively.

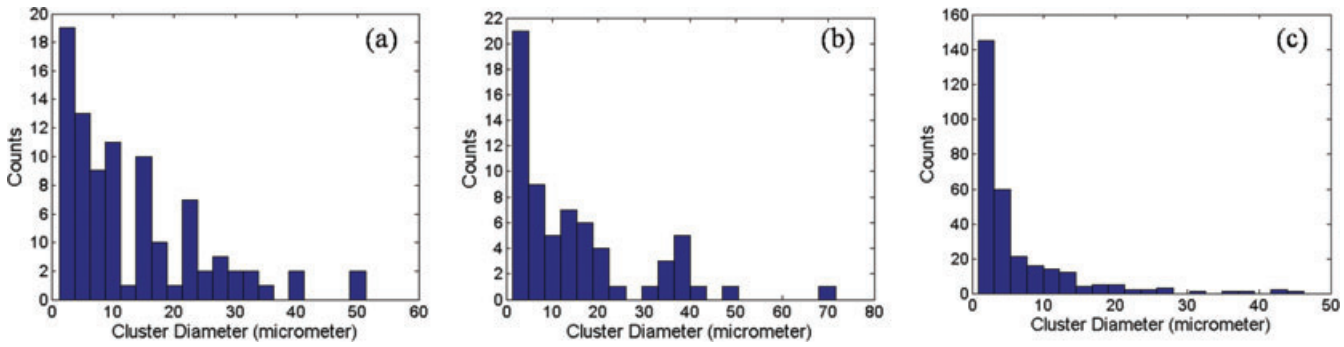

Fig. 9. Histograms show the distribution of the CMC-cluster diameters in PCL composites: (a) PCL 10, (b) PCL 30 and (c) PCL 50. As opposed to PCL 10 and PCL 30, the number of small sized (<5 µm) clusters is higher in PCL 50.

Table 2. Statistical parameters of CMC–polymer composites.

CMC content (wt%)	Average cluster diameter (μm)	Average aspect ratio	Population of clusters
10	13.1	1.8	89
30	14.7	5.8	65
50	5.8	1.8	295

geometrical properties of reinforcements. Here, the average diameter of CMC clusters, their population and their aspect ratios (the ratio of the size of the major axis to the minor axis in each particle) are summarized in Table 2.

The high population of small clusters and lack of good adhesion between CMC and PCL resulted in the lowest value of UTS in PCL 50 (Table 1) because the void formation rapidly increased and became the dominant failure mechanism. This observation is in good agreement with fractography analysis, where the fracture surface was much rougher in PCL 50 than other samples (Fig. 5d).

Another observation is that the size and population of clusters are not considerably different in PCL 30 and PCL 10. However, the clusters in PCL 30 had a much higher average aspect ratio as compared to the ones in PCL 10. Usually, higher aspect ratio reinforcements result in better stress transfer and improvement of mechanical properties (Azizi Samir *et al.*, 2005; Hamad, 2006). In this study, because CMCs did not make good adhesion with the polymer matrix, these high aspect-ratio particles acted as high stress-concentration areas, and resulted in failure at much lower loads. Finally, it should be mentioned that this statistical analysis was performed only on one vertical section from each sample. For more accurate analyses, it is necessary to employ stereology techniques (Russ & Dehoff, 2000) to extract 3D information from 2D images. As such, multiple cross-sectional images need to be analysed to represent a statistically valid conclusion.

Conclusions

SEM imaging and XuM were used to study the dispersion quality of reinforcements in polymer matrices, and their relationship with the overall mechanical properties of the composites. XuM images provided complementary information about the spatial distribution of CMC in PCL composites. This information can be used for better understanding of the behavior of variety of composite materials and further improvement of their qualities.

The spatial resolution of the reconstructed 3D volumes was sufficient to eliminate all suspicions about the quality of dispersion of the CMCs within the whole volume. Vertical slices through these volumes were used for statistical analysis on the size, shape and orientation of the CMCs.

The correlation of fractography and XuM data with the stress–strain curves revealed two mechanisms during the deformation of CMC–polymer composites. The size, shape and distribution of CMC clusters, had high effects on the void formation and crack propagation rates in the materials and weak bonding between CMC and PCL resulted in reduction of UTS in all composite samples. On the other hand, 10 wt.% CMC improved the flow of polymer molecules under stress and improved the ductility and toughness of PCL.

Acknowledgements

The authors thank Gatan Inc. (Pleasanton, CA) for providing the opportunity to use the X-ray ultra microscope (XuM), Dr. P. Mainwaring for critically commenting on this manuscript and Mr. M. LaCourt for helping with tensile tests. R.S.Y. acknowledges Michigan Technological University to provide seed funds to conduct this work.

References

Angles, M.N. & Dufresne, A. (2000) Plasticized starch/tunicin whiskers nanocomposites. 1. Structural analysis. *Macromolecules* **33**, 8344–8353.

Azizi Samir, M.F., Alloin, F. & Dufresne, A. (2005) Review of recent research into cellulosic whiskers, their properties and their applications in nanocomposite field. *Biomacromolecules* **6**, 612–626.

Batista, O.A. (1975) *Microcrystal Polymer Science*, McGraw-Hill Book Company, New York.

Bodenson, D. & Oksman, K. (2007) Dispersion and characterization of surfactant modified cellulose whiskers nanocomposites. *Compost. Interfaces* **14**, 617–630.

Bonse U. & Bush F. (1996) X-ray computed microtomography using synchrotron radiation. *Progress Biophys. Molec. Biol.* **65**, 133–169.

Choi, Y. & Simonsen, J. (2006) Cellulose nanocrystal-filled carboxymethyl cellulose nanocomposites. *J. Nanosci. Nanotechnol.* **6**, 633–639.

Cosslett, V.E. & Nixon, W.C. (1951) Improved resolution with the X-Ray projection microscope. *Nature* **168**, 24–25.

Cosslett, V.E. & Nixon, W.C. (1960) *X-ray Microscopy*. Cambridge University Press, London.

Dierick, M., Vlassenbroeck, J., Masschaele, B., Cnudde, V., van Hoorebeke, L. & Hillenbach, A. (2005) High-speed neutron tomography of dynamic processes. *Nucl. Instrum. Methods Phys. Res. A* **542**, 296–301.

Feldkamp, L.A., Davis, L.C. & Kress, J.W. (1984) Practical cone-beam algorithm. *J. Opt. Soc. Am.* **1**, 612–619.

Fleming, K., Gray, D., Prasannan, S. & Matthews, S. (2000) Cellulose crystallites: A new and robust liquid crystalline medium for the measurement of residual dipolar couplings. *J. Am. Chem. Soc.* **122**, 5224–5225.

Goldstein, J., Newbury, D., Joy, D., Lyman, C., Echlin, P., Lifshin, E., Sawyer, L. & Michael, J. (2003) *Scanning Electron Microscopy and X-ray Microanalysis*. Springer Science + Business Media, New York.

Grunert, M. & Winter, W.T. (2002) Nanocomposites of cellulose acetate butyrate reinforced with cellulose nanocrystals. *J. Polym. Environ.* **10**, 27–33.

Habibi, Y. & Dufresne, A. (2008) Highly filled bionanocomposites from functionalized polysaccharide nanocrystals. *Biomacromolecules* **9**, 1974–1980.

Habibi, Y., Goffin, A.L., Schiltz, N., Duquesne, E., Dubois, P. & Dufresne, A. (2008) Bionanocomposites based on poly(ϵ-caprolactone)-grafted

cellulose nanocrystals by ring-opening polymerization. *J. Mater. Chem.* **18**, 5002–5010.

Hamad, W. (2006) On the development and application of cellulose nanofibrillar and nanocrystalline materials. *Can. J. Chem. Eng.* **84**, 513–519.

Hon, D.S.N. (1994) Cellulose: a random walk through its historical path. *Cellulose* **1**, 1–25.

Jennings, B. & Parslow, K. (1988) K particle size measurement: the equivalent spherical diameter. *Proc. R. Soc. Lond.* **419**, 137–149.

Lapa, V.L.C., Suarez, J.C.M., Visconte, L.L.Y. & Nunes, R.C.R. (2007) Fracture behavior of nitrile rubber-cellulose II nanocomposites. *J. Mater. Sci.* **42**, 9934–9939.

Laiarinandrasana, L., Morgeneyer, T.F., Proudhon, H. & Regrain, C. (2010) Damage of semicrystalline polyamide 6 assessed by 3D x-ray tomography: from microstructure evolution to constitutive modeling. *J. Polym. Sci. B* **48**, 1516–1525.

Matsumura, H. & Glasser, W.G. (2000) Cellulose nanocomposites. II: Studies by atomic force microscopy. *J. Appl. Polym. Sci.* **78**, 2254–2261.

Maurer, H., Schubert, S.I., Bachle, F., Clauss, S., Gsell, D., Dual J. & Niemz P. (2006) A simple anisotropy correction procedure for acoustic wood tomography. *Holzforschung* **60**, 567–573.

Mayo, S.C., Miller, P.R., Wilkins, S.W., Davis, T.J., Gao, D. & Gureyev, T.E. (2002) Quantitative X-ray projection microscopy: phase-contrast and multi spectral imaging. *J. Microsc.* **207**, 79–96.

Mayo, S.C., Davis, T.J., Gureyev, T.E., Miller, P.R., Paganin, D. & Pogany, A. (2003) X-ray phase contrast microscopy and microtomography. *Opt. Exp.* **11**, 2289–2302.

Mele, P., Marceau, S., Brown, D., De Pudyt, Y. & Alberola, N.D. (2002) Reinforcement effects in fractal-structure-filled rubber. *Polymer* **43**, 5577–5586.

Myers, G.R., Paganin, D.M., Gureyev, T.E. & Mayo, S.C. (2008) Phase contrast tomography of single material objects from few projections. *Opt. Exp.* **16**, 908–919.

Nixon, W.C. (1955) High resolution X-ray projection microscopy, *Proc. R. Soc. Lond.. Ser. A, Math. Phys. Sci.* **232**, 475–485.

Oksman, K., Mathew, A.P., Bondeson, D. & Kvien, I. (2006) Manufacturing process of cellulose whiskers/polylactide acid nanocomposites. *Compos. Sci. Technol.* **66**, 2776–2784.

Russ, J.C. & Dehoff, R.T. (2000) *Practical Stereology*. Kluwer Academic/Plenum Publishers, New York

Siqueira, G., Bras, J. & Dufresne, A. (2009) Cellulose whiskers vs. microfibrils: influence of the nature of the nanoparticle and its surface functionalization on the thermal and mechanical properties of nanocomposites. *Biomacromolecules* **10**, 425–432.

Vaia, R.A. & Liu, W.D. (2002) X-ray powder diffraction of polymer/layered silicate nanocomposites: model and practice. *J. Polym. Sci. Polym. Phys.* **40**, 1590–1600.

Wang, B. & Sain, M. (2007) Dispersion of soybean stock-based nanofiber in a plastic matrix. *Polym. Int.* **56**, 538–546.

Weiss, P., Nihouannen, D Le., Rau, C., Pilet, P., Aguado, E., Gaitheir, O., Jean, A. & Daculsi, G. (2005) Synchrotron and non synchrotron X-ray microtomography three-dimesional representation of bone ingrowth in calcium phosphate biomaterials. *Eur. Cells Mater.* **9**, 48–49.